**How Bi-Modal are Jupiter's Main Aurora Zones?**

B. H. Mauk[1], J. R. Szalay[2], F. Allegrini[3,4], F. Bagenal[5], S. J. Bolton[3], G. Clark[1], J. E. P. Connerney[6], G. R. Gladstone[3], D. K. Haggerty[1], P. Kollmann[1], W. S. Kurth[7], C. P. Paranicas[1], A. H. Sulaiman[8]

1. The Johns Hopkins University Applied Physics Laboratory, Laurel, Maryland, USA (Barry.Mauk@jhuapl.edu)
2. Department of Astrophysical Sciences, Princeton University, NJ, US
3. Southwest Research Institute, San Antonio, Texas, USA
4. Physics and Astronomy Department, University of Texas at San Antonio, Texas, USA
5. University of Colorado, LASP, Boulder, Colorado, USA
6. Space Research Corporation, Annapolis, Maryland, US
7. Department of Physics and Astronomy, University of Iowa, Iowa City, Iowa, USA
8. School of Physics and Astronomy, University of Minnesota, Minneapolis, USA

## Contents of this file

## Introduction: Instrumental features of Juno JEDI data and users guide

Here we address the response of the Jupiter Energetic particle Detector Instrument (JEDI) on NASA's Juno mission to electron and ion distributions that are extreme in various ways (energy, intensity, angular structure, penetrating radiation, etc.). JEDI is documented in Mauk et al. (2017a), generated prior to Juno's encounter with Jupiter.

We consider first anomalies that occur within the JEDI electron measurements. Electrons are measured by JEDI using solid-state detectors (SSDs) that are 0.50 mm thick and that are attached on the back to a thick shield of Tungsten-Copper (that can redirect some escaping electrons back into the SSDs). The fact that some electrons can fully penetrate and leave the detector causes a distortion in the measured spectra. We have developed a procedure described here to correct the contaminated spectra. This same procedure provides a method of clearly discriminating between sharp features caused by auroral acceleration and sharp features that can be caused by the penetrators. This same procedure also provides a technique for identifying regions of saturation, where the sensor cannot process electron events fast enough to reconstruct the original spectral shapes at the lower energies. We also address the issues of very high energy electrons that penetrate the sides of the sensor volume, and the measurement of very narrow electron angular features. For electrons, we finally address the issue of the occasional proton contamination of the electron distributions.

We also address here issues related to the measurement of ion distributions. Ion measurements are more robust than electron measurements because of the use of coincident circuitry. Here, multiple, near simultaneous, signals must be received before an event is considered valid. However, the circuitry can be overwhelmed with what are termed "accidentals", whereby the multiple elements of the coincident circuitry can be overwhelmed with random events.

We finally provide a list of additional features of which users must be aware before using JEDI data.

**Text S1. SSD electron penetration contamination of electrons**

Here we present the procedure that we use to correct the JEDI-measured electron spectra that are contaminated with high energy foreground electrons that penetrate the detector. By foreground we mean electrons that entered by means of the appropriate collimator openings. This issue is different than the one regarding the electron penetration of the side walls of the JEDI instrument (See Text 5), although such side-wall penetrating particle will contribute to the process described here.

The minimum energy of an electron that can fully penetrate the JEDI SSDs is about 400 keV. If an electron penetrates the detector, it does not deposit all of its energy in the detector and therefore the deposited energy does not correctly characterize the measured electron. While electrons above 400 keV can penetrate the detector, many do not because electrons scatter within the detector, so that electron energies much higher than 400 keV can be measured on a statistical probability basis. Effectively, the measurement of electrons above 400 keV can be book-kept by using an efficiency. The drop in efficiency for electrons with energies that exceed the penetration depth of the solid state detector has been determined empirically and is parameterized here as an efficiency.

$$Effpen = 1 - Exp\left[-2\left(\frac{480}{EkeV}\right)^3\right] \qquad (1)$$

where EkeV is the kinetic energy of the incoming electron. The technique for empirically establishing this expression and the expressions that follow was to run the entire procedure described here on many different spectra while the varying the parameters of the expressions. Success was declared when good fitting results were achieved with a single set of parameters for wide diversity of spectral shapes and intensity values. Note that this high energy tail correction to the JEDI data (Equation 1) was not applied to the archived JEDI data for data collected early in the mission. Later in the mission it has been applied. Data generated since we started doing this correction as part of the processing have a keyword EFFCOR. If it is set to T, the correction has already been applied. If it is set to F, or if that keyword is missing altogether, the correction was not applied. This is a reliable way to know for sure whether the high energy tail was corrected on a file-by-file basis. And so, to apply the full procedure describe here for data processes with the Equation (1) correction, one must first remove the correction given with Equation (1), or otherwise be aware that that correction has been made.

Every electron that fully penetrates the detector leaves behind a contribution to the minimum ionizing bump in the spectrum (Figure S1A). In other words, the count rate in the vicinity of 160

2

keV is the sum of the count rate of electrons at that energy and the count rate of penetrating electrons that deposit that much energy before they exit the SSD. The shape of the minimum ionizing feature is insensitive to the shape of the penetrating electron spectrum because the energy deposition per unit distance (the so-called dE/dX function, called the stopping power) is very flat at these energies (Zombeck, 2007). But, it is not exactly flat, and there are other details (degree of scattering for penetrating electrons with different energies) that lead to some small dependencies of the minimum ionizing peak to the penetrating spectrum. At this point in the development, we assume that the shape of the minimum ionizing spectrum is universal and unchanging. It has been determined empirically and is parameterized here with the following analytic equation:

$$MIfunc = \frac{Func1 \; x \; Func2}{35.47} \tag{2}$$

where
$$Func1 = \frac{(1 + Tanh[0.1\,(EkeV - 112)])^2}{4}$$

$$Func2 = Exp\left[\frac{-(EkeV - 85)}{60}\right]$$

Here the "35.47" is the normalization factor that makes the area under MIfunc equal to 1 (the reason for this factor will become apparent below). This function does not perfectly reproduce the bump in the observed spectra. For the reasons described above, we find that sometimes the peak of the observed minimum ionizing function is slightly higher or lower than the peak parameterized here.

Our procedure is to use a parameterized functional form for the input energetic electron spectrum. The form that we use is from Mauk and Fox, (2010, for electrons), which is a kappa distribution normalized with an additional power-law break at higher energies. Note that we use this function only for energies greater than about 78 or 90 keV (spectrum dependent); we leave the points below that energy unchanged since those energies have nothing to do with the effects that we are trying to model. The spectrum has the form:

$$Intensity = \frac{C \; EkeV \; [kT \, (g1 + 1) + EkeV]^{(-g1-1)}}{\left[1 + \left(\frac{EkeV}{Eo}\right)^{g2}\right]} \tag{3}$$

where EkeV is energy in keV. Here the free parameters that we must optimize are C, kT, g1, Eo, and g2. The units on the intensity are $1/(cm^2 \; s \; sr \; keV)$.

In the procedure developed here, we keep a careful accounting of particles that are lost and gained. Every particle that is lost (not counted at its actual energy) because it penetrates the detector shows up as a single particle contribution to the minimum ionizing peak. We therefore must know how many particles are lost, not just within the nominal energy range of JEDI, but to much higher energies as well. We therefore must determine the following integral, where PLost is the number of electrons per time that are not detected close to their actual energy, over the area and solid angle of the instrument.

3

$$PLost = \int_{Elow}^{Ehigh} Intensity \; x \; (1 - Effpen) \; dEkeV \qquad (4)$$

from Elow (any energy that is lower than those that can penetrate the detector; e. g. use 30 keV) to Infinity (or a very large number, Ehigh). *Intensity* (Equation 3) refers to the ambient (not measured) distribution of electrons and describes their number at their actual energy, per time, energy range, detector area and solid angle. Note that if the power law of the high energy tail of the incoming electron distribution at the highest energies (g1 + g2 for Equation 3) becomes small enough (close to the value of 1) then the parameter PLost becomes unconstrained (diverges as one integrates to infinity) and the procedure fails.

The procedure now is to optimize the parameters in Intensity (Equation 3) such that we fit the observed spectrum with the following function:

Fit = Intensity x Effpen + PLost x MIfunc (5)

The factor Effpen removes electrons from their ambient energy within the high energy tail, and the second term adds these electrons into the minimum ionizing feature.

Just as an example, this procedure is easy to implement for single spectra in the software Excel using the Solver subprogram (sample available on request). An example of such an optimization for a highly contaminated spectrum is shown in Figure S1A. Here the individual blue symbols are the original data, the solid blue line is the fit (Equation 5) to the data for energies greater than 78 keV. The red line is the input spectra (Equation 3) that has had its parameters optimized to yield the best fit of the blue solid line to the data (blue symbols). The final result (shown in Figure S1B) comprises the original data for energies up to about 90 keV, and the reconstructed data using the red line for energy greater than or equal to 78 keV.

There are tricks to obtaining the most robust fits over all energies. Our error function that must be minimized uses the logarithm of the intensity values (Error = Sum[Log(model) − Log(data)]²). A robust procedure sometimes requires that the sensitivity of the error function to the various parameters be flattened out. One way of doing that is to rewrite Equation (3) into something like:

$$Intensity = \frac{10^{LC} \; \frac{EkeV}{100} \left( \frac{kT}{100} \; (g1 + 1) + \frac{EkeV}{100} \right)^{(-g1-1)}}{\left( 1 + \left( \frac{EkeV}{Eo} \right)^{g2} \right)} \qquad (6)$$

Here, the energies have been normalized by an energy parameter (100 in this case) that is contained within the range of energies under consideration, a normalization that reduces the sensitivity of the error function to the g1 parameter. In this version we are also optimizing the log of the normalizing parameter (LC) rather than the normalizing parameter itself (C), thereby increasing the sensitivity of the error function to the normalizing parameter.

4

**Text S2. SSD penetration effects on electron moments**

Here we discuss the effect of electrons that fully penetrate the JEDI solid state detectors on the calculation of moments of the electron distributions.

An important parameter for addressing the impact of energetic electrons on auroral physics is the energy flux that precipitates down onto the atmosphere. The procedure for calculating this parameter has been described elsewhere (Mauk et al., 2017b). But, an important consideration is how that parameter might be modified by the distortions that arise from the penetrating particles. It turns out that if we do no correction, and just use only the original uncorrected data (including not applying equation 1, which is sometimes already applied to the archived data), we obtain a lower limit to the energy flux for electron energies >30 keV. That outcome occurs because the electrons that are lost within the >400 keV higher energy tail (including those above the nominal energy range of JEDI) are all counted, but their energies are reassigned to a lower value, close to 160 keV. Figure S2 shows, in black, the "lower limit" to the energy flux described here (this figure is the top panel of Figure 3 in Mauk et al.; 2018). Note that the number flux that one would obtain by simply integrating the original uncorrected data will be close to the correct value for >30 keV electrons, since the energy assigned to the particles is not relevant to that parameter, provided they are not assigned an energy lower than JEDI's energy range. Only the very small percentage of > 1.2 MeV electrons that are fully stopped by the detector are not counted because there is no channel accumulation for such electrons. Hence a characteristic energy (Ec), defined as the ratio of energy flux to number flux, is also a lower limit, when using uncorrected data.

In order to further constrain the energy flux in an automated way we have, in Figure S2 and shown in red, partially corrected the data by applying the efficiency factor in Equation (1) but not trying to subtract off the minimum ionizing peak. The integral of that partially corrected spectrum yields an upper limit to the energy flux with respect to integration over energy. Hence, Figure S2 shows both a lower limit and an upper limit, to the extent that the spectra are not saturated (see Section S4). We see that these two limits are fairly close to each other, such that the energy flux moment is fairly well constrained.

**Text S3. Distinguishing electron auroral acceleration from electron SSD penetration**

Here we discuss the procedure for cleanly distinguishing between the sharp spectral feature that is caused by high energy electrons that penetrate the JEDI solid state detectors and the sharp spectral features caused by auroral acceleration.

Figure S1A shows that penetrating electrons give rise to a peaked feature that might potentially be mistaken for coherent auroral acceleration. But, what we have found is that when a true coherent auroral acceleration occurs, it is seldom accompanied by a high energy tail sufficient to give a substantial minimum ionizing peak. The procedure documented in Section S1 can be used to test this premise. Figure S1C shows an example where a strong auroral acceleration feature is present (this is spectrum 5 in Figure 5 of Mauk et al., 2018). Here we have run our procedure but have artificially eliminated the data points between about 130 and 350 keV (corresponding to the auroral acceleration feature) to see how much of a minimum ionizing peak the high energy tail can produce. The minimum ionizing contamination is the very small bump that represents the difference between the solid blue line and the solid red line. This

bump is clearly different from the main peak shown in the unconnected symbols, and therefore, for this case, inconsequential for characterizing the auroral acceleration feature.

## Text S4. Electron measurement saturation

Here we discuss a procedure for determining when the JEDI electron sensors become partially saturated by particle intensities that are higher than the instrument can fully process.

Electron events within JEDI are processed by an onboard computer that can process up to about 30,000 events per second. Fast field-programmable gate array (FPGA) based counters, and so-called dead time counters, are used to renormalize the channel rates on the ground, allowing for the proper reconstruction of the electron spectra for rates approaching $10^6$ counts per second. For even faster rates, proper reconstruction of the spectral intensities and shapes becomes more difficult. The same procedure, documented in section S1, can be used to identify regions where the intensities are too high to be fully quantified by the JEDI sensor, essentially checking for self-consistency of the measurements. An example is shown in Figure S1D (this is spectrum 2 in Figure 5 of Mauk et al., 2018). Here we have blindly applied our spectra correction procedure, and the procedure clearly fails since the blue curve does not match the blue symbols. The high energy tail of the distribution is demanding that there exists a minimum ionizing bump near 160 keV, but the bump is simply not there. In this case the counts per second summed from all of the channels, nominally corrected for a dead time, sum to 1.4E6, outside the nominal count rate range of the sensors. Electronic pulses within the instrument, stimulated by the individual electron events, are landing on top of each other, and the instrument is not able to correctly detect every particle and identify the appropriate bin for each measured event. And more specifically, the energies of the identified events that are binned are smeared out to some extent, particularly at the lower energies. This process has likely broadened the expected minimum ionizing peak (blue curve in Fig S1D) to the observed distribution (blue symbols).

Note that JEDI was designed to mitigate the problem of saturation should it be determined that a substantial fraction of the main auroral crossings would result in saturation. JEDI SSDs for each of the three instruments have both large and small pixels (with only large or small pixels active at any one time for each species, electrons and ions; Mauk et al., 2017a). The saturation documented here occurred with large pixels. Going to small pixels reduces the count rates by about a factor of about 12 (determined empirically; the apparent area difference is a factor of about 20, a factor that does not take into account SSD edge effects). During Juno's first auroral pass (PJ1) large pixels were used in JEDI-90 and small pixels were used in JEDI-270. Saturation was not detected during PJ1 and thus the decision was made to utilize large pixels on many follow-on subsequent orbits. Small pixels have been used for some later orbits.

## Text S5. Electron side-wall penetration effects on electrons

Here we discuss how to distinguish contamination within the JEDI electron sensors that occurs as a result of electrons that have energies high enough to penetrate the detector shielding, and often sideways with respect to the detectors and the collimated beams of foreground electrons. Electrons with energy greater than about 10 MeV can penetrate the cylindrical blades that make up the JEDI collimator (see the Appendix of Mauk et al., 2017a). Electrons with energies greater than about 15 MeV can penetrate the side shielding of JEDI (*Ibid*).

Electrons with energies high enough to penetrate these structures certainly exist within Jupiter's hard radiation regions. Mauk et al. (2017b) identified where such penetrators are important for perijove 1 (PJ1).

The so-called "witness" detectors (Mauk et al., 2017a) offers the most important indicator of side-penetrating electrons. These witness detectors are found in the data product designated as "Ion Energy Spectra" data from the JEDI sensor JEDI-A180 (the word "ion" is misleading because these nominally ion detectors are responding mostly to electrons). The small-pixel ion SSDs in the JEDI sensor JEDI-A180 serve the purpose described here, and for most of the mission, these sensors were commanded into the small pixel configuration, particularly close to the planet. Three of 6 of these pixels (telescopes T2, T4, and T5) are bare and measure foreground electrons with energies greater than about 25 keV. Two of the 6 pixels (telescopes T1 and T3) have thin shields covering them (0.64 mm titanium). These pixels measure foreground electrons with something like > 1 MeV on average; the extrapolated range corresponds to ~0.76 MeV). (Pixel "0" is bare but is partially blocked by a sun shield and is not used for these analyses; its response is typically between that of the shielded and unshielded detectors.) In non-penetrating environments, the shielded and unshielded witness detectors show different responses. However, when the dominant inputs that these 6 pixels are receiving are from side-penetrating electron radiation, all of the sensor see essentially the same output. The bottom panel of Figure s3 shows a characteristic example. This is just a plot of total summed counts received by each witness SSD (being careful not to include the very lowest energy channels, well below the energies required of JEDI, that can be contaminated with detector noise). Here, Juno is traveling in Jupiter's inner magnetosphere, moving inside of the Moon Io's L-shell. On the left of the figure, well outside of Io's orbit, telescopes T2, T4, and T5 are well separated from telescopes T1 and T3, indicating that good foreground measurements are being made. That conclusion is reinforced by the observations in the 3rd panel of clear dynamic electron injection signatures. However, on the right side of the panel the 5 telescopes all pinch together, indicating that these sensors are all overwhelmed by side penetrating electrons. Hence, the electron spectra shown in the 3rd panel of Figure S3 is judged to be fully contaminated in this region. Note that JEDI, designed to measure Jupiter polar phenomena that magnetically map to regions near and outside of Europa's orbit, was not designed to make measurements near Io's orbit. However, the ion measurements (2nd panel) are judged to be relatively clean, even while revealing some "accidentals" contamination in the lowest intensity regions (as discussed in Section S9).

We have several warnings about the use of the witness detectors. First, the process described here is only available when the JEDI-A180 ion SSDs are in their small pixel modes (That is the most likely orientation but there might be times when this is not the case). Second, because of scattering within the measurement volume of JEDI, the shielded witness detectors (T1 and T3) actually measure about 8% of the > 25 keV, non-penetrating foreground electrons. Quantitative use of the witness detectors must take this scattering component into account. For example, the maximum contrast between the shielded and unshielded detectors will be something like 8/100 = 0.08. The pitch angle structure can complicate these measurements. Specifically, over the poles, where even side-penetrating electrons can occur in the form of magnetic field-aligned beams, it is sometimes observed that the shielded detectors have even higher rates than do the unshielded detectors. This situation occurs when the orientation of the sensor is such that the beaming penetrating electrons come through the JEDI collimator and illuminate one of the shielded SSDs to a greater extent than they do the unshielded

sensors. In strongly beaming situations, the witness detector system can be difficult to interpret. Note that the unique characteristics of the witness detectors can also be used to provide a scientific metric of the environment, as shown by Paranicas et al. (2018) in measurements over Jupiter's poles.

There are other indicators of strongly penetrating electrons. As documented in Paranicas et al. (2017) and Kollmann et al. (2017), the presence of penetrators in a given energy channel can be identified in regions close enough to Jupiter to where JEDI resolves the loss cone. The upward loss cones should be empty in the radiation belts unless the detectors are contaminated with side penetrators. Elsewhere and where the external distributions have non-isotropic pitch angle distributions, unnatural patterns emerge in the electron pitch angle distributions whenever side penetrators are playing a role. This issue is most important very close to Jupiter when Juno passes the horns of the hard radiation belts. Another indication of the importance of side penetrating electrons can be derived by applying the procedure documented in section S1. Even electrons with energies >15 MeV will contribute to the generation of the minimum ionizing feature. Thus, the procedure places constraints even on electrons with energies sufficient to penetrate the sides of the sensor. The feature in the 3$^{rd}$ panel of Figure S3 labeled "e- penetrators" is the minimum ionizing signature of side penetrating electrons.

## Text S6. Electron angle resolution issues

Here we discuss issues that arise with the JEDI electron measurements when the features that are being observed are more structured in angle than can be resolved by the JEDI fields-of-view.

The instantaneous full-width-at-half-maximum field of view (FOV) of the JEDI electron telescopes is about 9°x17°. The accumulation time for each high rate sampling (the mode that JEDI always uses near the planet) is about 0.5 seconds, corresponding to about 1/60 of a rotation, or about 6° or rotational motion, roughly in the direction that corresponds to the "17°" dimension in the FOV. There are narrow angular beams that JEDI has observed, particularly in the upward direction over the polar cap (Mauk et al., 2017a; see Figure S4). JEDI does not resolve these beams. JEDI's derived intensities will be low for such beam for two different reasons. First, if one generates pitch angle distributions with resolution elements that are too coarse (e. g. 15 degrees), then some observations will be included in the field-aligned accumulations that do not have the magnetic field line contained within the FOV at any time during the accumulation. For the very narrow beams, one should utilize pitch angle resolutions in the plots as narrow as 4.5 degrees to make sure that any accumulation purporting to be in the field-aligned direction actually includes the field line within the accumulation. For a 30 second accumulation (one spacecraft spin), the somewhat offset configuration of the JEDI viewing often allows resolutions down to 4.5 degrees. But there will also be time gaps. For shorter time accumulations it is rare that viewing down to within 4.5 degrees of the field line can be achieved.

It has turned out to be very fortunate (and also physically significant in a way that we do not yet understand) that the downward going electron intensities over the main aurora are often much broader in angle than the upward going intensities in some main aurora regions. Various analyses have shown that often one may average over, say, 15 degrees without engendering substantial spin modulation in the downward fluxes. However, for the analysis of any particular

period of time, the researcher must perform a number of different experimental tests with the data to make absolutely sure that there is not an angular sampling problem. Such experiments involve plotting and re-plotting the data using a wide variety of combinations of time resolution and angle resolution to see how the character of the plots changes. For example, does one get a sudden burst of energy flux only at the instance when the pitch angle coverage is particularly complete and not elsewhere?

Missing the field line is only one of the ways that intensities might be in error. The second reason that JEDI intensities of beams are a lower limit is this: when we convert count rates into intensities we assume that the FOV of the instrument is uniformly filled. For narrow beams, such as the upward beams over the poles, the FOV is not filled because JEDI does not resolve the beams. Under this circumstance the apparent intensities and energy fluxes will be lower than they should be. No correction has been applied to the JEDI data to mitigate these occurrences.

## Text S7. Electron internal scattering

Here we discuss the issues that arise with the JEDI electron measurements as a result of electron scattering within the JEDI sensor volume.

One of the driving requirements for the JEDI instrument was to be able to obtain nearly complete pitch angle distributions at every instant of time (0.5 second distributions). Because of the rapid motion of the spacecraft (up to 55 km/s) and the slow rotation of the spacecraft (2 rotations per minute), a multiplicity of simultaneous look directions is required. To obtain the needed number of look directions using limited resources, it was necessary to allow the trajectories of the particles to share a common sensor volume (Mauk et al., 2017a). When electrons enter the sensor volume of JEDI, some of them can hit internal structures within the sensor other than the SSDs. A fraction of those electrons can scatter and find their ways to other SSDs from directions that were not intended with the sensor design. This mechanism limits the contrast that can be seen within highly structured features, such as strongly magnetic field aligned beams. Figure S4 shows some example electron pitch angle distributions (30 – 1000 keV) that reveal the character of scattered component. These are measurements of very narrow, magnetic field-aligned electron beams within Jupiter's polar caps (Mauk et al., 2017b). The left hand plots show that the scattered component exists at something like the percent level. However, an aspect of the response that requires special vigilance is the situation where the electron beam enters the detector from a direction that is not quite ideal; that is the center of the angular beam does not hit the center of the SSD. Rather, parts of the beam are aimed at structures that are off to the side of the SSD. In these cases, the contrast between the measured beam and the scattered component can be less than the 1% mentioned above. For example, the plot on the right of Figure S4 shows a contrast (signal to noise) at the 5-10% level. Such low signal-to-noise situations can happen when JEDI does not angularly resolve the features of interest (see also section S6). Much care must be exercised in analyzing these very narrow features.

## Text S8. Contamination of electrons by protons.

A 2 mm aluminum flashing covers the entrance surface of the electron SSDs. This flashing is intended to protect the electron detectors from proton contamination. It also limits the

electron SSD response to electrons with energies greater than about 25 keV. But, protons with energies greater than about 300 keV can contaminate the electron measurements. Such contamination is rare because typically the electrons are much more intense than are the ions (one such rare example from the magnetosphere is shown in Fig. S5), except for the region of the innermost radiation belt, where this result is the norm (Kollmann et al., 2017).

Use Table S1 to compute the level of contamination. One compares the intensity of the protons (that is measured without ambiguity through the TOFxE coincidence) at the energy in the first column with the nominal electron intensity (that in reality is a total particle measurement of ions and electrons) at the energy of the middle column. That middle column energy is the energy that a proton will have after it penetrates the aluminum flashing and the several very thin foils that the proton encounters prior to encountering the flashing. If the electron intensity is much larger than the proton intensity for that pair of energies, then there is little or no contamination of the electrons by the protons. If the intensity numbers are close, then one needs to do a more accurate job. For a more accurate determination, one needs to compare the Phase Space Densities at the pair of energies under the assumption that the electrons are protons. That means comparing intensity divided by energy in the non-relativistic regime ($I/E$); or momentum squared in the relativistic regime ($I/p^2$), for the pair of energies. That procedure gives a very small boast to the electrons, making contamination just a little less likely (but not much).

**Text S9. "Accidental" contamination of ion measurements.**

Ions are measured with a coincidence system. For the low energy "time-of-flight by pulse height" (TOFxPH) measurements, a valid event is one that has both a "start" generated by electrons coming out of a "start foil", with secondary electrons striking portions of the JEDI microchannel plate (MCP), and a "stop" generated by electrons coming out of a "stop foil" with secondary electrons striking another portion of the MCP. The "start" and "stop" must both occur within a time window of no greater than about 150 ns, the longest relevant time-of-flight for the JEDI measurements. For a higher energy "time-of-flight by energy" (TOFxE) measurement an additional 3rd signal is required within an additional time window, a signal from one of the solid-state-detectors (SSDs). The time window for that 3rd signal to occur with respect to the time-of-flight signals is about 150-300 ns, a range that results from an uncertainty in our present knowledge (see discussion below). Both of these measurements are immune to low levels of penetrating electrons because any one such electron can generally only stimulate one of the two or three needed signals.

However, once either the penetrating electrons become overwhelming, or the system is overdriven even by non-penetrating particles (electrons or ions), the required multiple signals can be stimulated by separate, randomly occurring particles within the time windows specified in the preceding paragraph. The result is contamination of the measurements called "accidentals". Such contamination is apparent in the right-hand-side of the proton measurements of Figure s3 with features labeled "e- ". And the top panel of Figure S3 shows a region of heavy ion measurements that are fully contaminated with accidentals caused by electrons. These types of contaminations are particularly severe within the horns of the electron radiation belts over the poles. In Figure S6 (Figure 3 of Mauk et al.; 2017b), an apparent entire false proton population (second from the bottom panel) occurs between 1220

and 1235m and between 1300 and 1320. Note that TOFxPH data, with only 2 coincident signals, is particularly sensitive to accidental contamination. That is one reason why the TOFxPH data is under-utilized in JEDI publications.

For TOFxPH data, we are focusing on proton channels only, since the large effort needed to quantify the heavy ion channels has not yet been performed. The rate of accidentals contaminating a TOFxPH energy channel is the rate of directional (within a specified telescope direction) start events (RD[start]) times the probability of a random (uncorrelated) stop event occurring within the relevant time window. The "D" in the parameter designation is clarified below. The relevant time window depends on the goal that we are trying to achieve. If we are looking for contamination within the entirety of the TOFxPH measurements, we need to use longest acceptable TOF, 150ns. Usually however we are interested in the accidentals within a given energy range that is established by a range of TOFs. In that case the window for an individual energy channel is $t_2-t_1$, where $t_2$ and $t_1$ are the TOFs that correspond to the low and high energy boundaries of that particular channel. Tables S2 and S3 can be used to estimate these respective times. Table S2 provides the coefficients of $6^{th}$ order polynomial fits to the TOF versus input energy for each mass species. Table S3 shows some calculated values from those polynomial fits (some nonsense numbers occur outside of the nominal energy ranges of the sensors). The rate of accidental TOFxPH contamination for a give energy channel (call it RD1) is:

$$RD1[accidental] = RD[start] \times \{1-Exp[-RD[stop] \times (t_2-t_1)]\} \qquad (7)$$

Here, the exponential factor is the Poisson probability of getting zero counts within the time window. Hence, one (1) minus the exponential is the probability of getting one of more counts within the time window. When $RD \times (t_2-t_1) < 1$ one can expand the exponential and keep only the first two terms in that expansion, yielding:

$$RD1[accidental] = RD[start] \times RD[stop] \times (t_2-t_1) \qquad (8)$$

That expansion may not always be valid, but for JEDI, saturation effects would likely come into play for such situations. A complexity in determining the directional starts and stops rates (RD) is that the data stream reports only a total start R[start] and stop rate R[stop], for the entire instrument, comprising 6 different telescope look directions (Future instrument generations would benefit from reporting each RD). R[start] and R[stop] are provided in the TOFxPH and TOFxE data sets. For accidentals caused by hard-radiation penetrators, where the source of the accidentals is roughly isotropic, one would use RD[start] = R[start]/6, and RD[stop]=R[stop]/6 for a total reduction in the accidental rate or 1/36 if, in Equations (7) and (8), RD is replaced with R/6 in all cases. Empirically we have found that 1/25 works better when dealing just with TOFxPH, likely due to the fact that even penetrating electrons are more effective when they come through the collimator and collimator blades rather than when they fully penetrate the instrument sides. (That condition is likely why even fully accidental populations (Figure S6) show apparent loss cone distributions.) Note that the condition that the stop sector must match the start sector for an event to be considered valid is a parametric choice in JEDI. It allows the condition RD[stop] = R[stop]/n (where n is 5 or 6), thereby reducing the accidental rates substantially. That is because the "stop-direction must match the start-direction" condition allows the 6 different look directions to behave as if they are 6 fully-independent telescopes, each with their own start and stop rates. If the particles that cause the accidentals

rate are highly anisotropic, then the procedure described here to relate RD to R will not work, and it will be exceedingly difficult to use Equation (8) to determine accurate levels of contamination.

Fortunately, for TOFxPH proton data, it is generally unnecessary to do this kind of detailed calculation. For this data product, accidentals yield a universal spectrum that is very easy to identify, as can be seen in Figure S7a and S7d. That spectrum, expressed as an intensity versus energy, is approximated with the following polynomial form, again for protons:

$$Log_{10}(I_{acc}) / Log_{10}(C) = -1.9345 \times LE^3 + 9.9785 \times LE^2 - 18.9779 \times LE + 13.3799 \quad (9)$$

where $I_{acc}$ is the accidentals intensity, C is a normalizing constant, LE = $Log10(E_{keV})$, and $E_{keV}$ is energy in keV. The procedure to testing the presence of accidentals is to vary C and see if the low energy portion of the spectrum matches the accidentals spectrum shape, a shape that is unlikely to be reproduced by natural events. That condition is seen to be true in Figures S7a and S7d. In both cases for the lowest energies, equivalent to the largest t2-t1 window (coinciding with the longest TOFs), it is most likely to get an accidental event. We note also that the efficiency for the detection of true signal H+ between 5 and 10 keV is so low, that any counts that exist within that energy range represents a signature that accidental counts are present. Equation (9) is derived by assuming that accidental counts are proportional to (t2-t1) and then calculating the channel intensities on that basis using each channel characteristics.

Accidental contamination is strongly suppressed if the solid state detectors are stimulated (representing the TOFxE data product). And so, one of the first things to do in assessing accidental contamination in the TOFxE data is to check whether the higher energy TOFxPH channels are contaminated using the technique described in the previous paragraph. If those higher energy TOFxPH channels are uncontaminated, then the TOFxE data for the same look directions are also certainly uncontaminated. But, if TOFxPH is fully contaminate as it can be close to the planet, more effort will be required, as described below.

By adding the 3rd signal from the SSDs, one obtains (call it RD2):

$$RD2[accidental] = \{RD[start] \times RD[stop] \times (t2-t1)\}* RD[SSD-\Delta E] \times T[SSD-Int] \quad (10)$$

where the final portion (beginning with RD[SSD-$\Delta$E]) also began as a Poisson exponential (like that in Equation 7) and was expanded and truncated to yield the results shown here. Here, RD[SSD-$\Delta$E] is the raw counts measured by the relevant directional SSD within the relevant energy band, and T[SSD-Int] is the SSD coincidence time for identifying an event. RD[SSD-$\Delta$E] is not provided within the TOFxE data product, and estimates of this parameter must be found elsewhere (see a later paragraph). Formally the SSD integration time is something like 150 ns, but empirically we have found that a coincidence time like 280 ns is needed in the equation for T[SSD-Int] above to give the accidental rates that we see in data like that presented in Figure S3 (top).

To estimate RD[SSD-$\Delta$E], energy-resolved rates of unshielded SSDs are needed through the "ion spectra" and "electron spectra" products. These products may be available for the same JEDI unit, otherwise a neighboring JEDI will need to be used. Important here is that the SSD-

only channel(s) selected need to be associated with the same energy deposited in the SSD as the TOFxE channel. Tables S4 and S5 provide the needed conversions. For example, if one is looking for the accidental rates in an Oxygen channel, one would look for the range of energies involved with that channel in the second to the last column in Table S5. Then, if one is using a bare detector, like the uncovered witness detectors (JEDI-A180 "ion energy spectra"), one would use the count rates in those witness detectors interpolated and summed over the range of energies in the left-hand column for those detectors to estimate R[SSD-$\Delta$E]. Interpolation and perhaps summation is needed because the witness detector energy channels are unlikely to match the needed range of energies. If one uses the electron detectors rather than witness detectors, one would obtain the needed range of energies from the 3$^{rd}$ column of Table S4 rather than from the left-hand column.

The final accidental rates that contaminate an TOFxE ion energy channel caused by highly penetrating radiation is:

$$RD2[accidental] = \{(R[start]/5 \times R[stop] /5) \times [(t2-t1)]\} \times R[SSD-\Delta E] \times (0.28\ E\text{-}6\ s) \qquad (11)$$

where the here we have replaced RD with R/5 for both the starts and the stops based on the discussion just following Equation (8). We have also converted the 280 ns into seconds. Note that the parameters used here (e. g. "5", "0.28E-6") are based on the examination a just several data periods. A more extensive examination may lead to modifications in these parameters.

If the TOFxE accidentals are caused by highly directional electron populations, it will be almost impossible to determine the relationship between RD and R and therefore derive a directional correction to the measured rates. From Figure 9 in Mauk et al. (2017a) we know that it is the lower energy electrons that interact most with the foils and microchannel plates of JEDI to generate the signals that end up as accidentals. JEDI does not measure electrons with the energies that likely cause the accidental signals through a dedicated measurement such as that obtained with SSDs. Because electrons below 2-3 keV are rejected from JEDI with electrostatic potentials, it is electrons with energies close to 3 keV that will likely dominate the generation of accidentals. An absolute worst case estimate of accidental rates when the cause of the accidentals is strongly anisotropic would be to a assume that RD = R for both the starts and the stops. Given strong scattering within the start foils, a more rational worst case might be RD[start] = R[start] and RD[stop] = R[stop]/5.

The red dashed line in the top panel of Figure s3 shows an Equation (11), R2 calculation for the particular channel in question there (with the calculated rate converted to an intensity using channel characteristics). The identification of the one region that appears to be completely dominated by accidentals was used to tweak some of the parameters in our equation. Note that the accidental rates are to be compared with the observed rates within each respective channel. JEDI data contains not only intensities for each channel but the counts per accumulation (raw and uncorrected) and the count rate (corrected for instrumental characteristics). The calculated accidental rates should be compared to the corrected count rate (or converted to an intensity to compare with that as we have done in Figure S3).

Although it is not needed under the assumption that electrons are the cause of the accidentals, it should be recognized that the "deposited energy" shown in Tables S4 and S5 is not the same as the "measured energy" reported to the JEDI electronics. The measured energy requires (for

just the ions and not the electrons) a "pulse height defect" term, which makes the measured energy less than the deposited energy.

**Text S10. Miscellanea**

1. JEDI contains many data products, some of which were invented to fit JEDI data within limited data volumes. For each of the 3 JEDI sensors (J90, J270, J180) there are data products for Low Energy Resolution Electrons, High Energy Resolution Electrons, Low Energy Resolution time-of-flight x energy protons (TOFxE), High Energy Resolution TOFxE protons, Non-Proton TOFxE Heavy Ions, Low Energy Resolution time-of-flight x pulse-height protons (TOFxPH), High Energy Resolution TOFxPH protons, Non-Proton TOFxPH Heavy Ions, Low Energy Resolution "Ion" Spectra (usually dominated by electrons), and High Energy Resolution "Ion" Spectra (also usually dominated by electrons). The Witness Detectors are found in the JEDI-A180 "Ion" Spectra Data Products, but are useful as witness detectors only when the ion sensors are in small pixel mode. Because of problems with high voltage on JEDI-A180, TOF data is not taken on that unit. A reliable way to determine which data products are available at any one time is to go to: http://sd-www.jhuapl.edu/jedi/data/webapp/. There one may set at date, a JEDI unit, and select "DATA_PRESENT". This web site is also very useful for getting a summary about how the JEDI units are responding to the jovian environment. With the generation of any particular data product described here, there are parameters that are set to adjust data volume. These parameters include time resolutions, sector averaging (out of the nominal 60 sectors per spin), and even multiple spin averaging.

2. True ion data are found ONLY in the data products whose file names contain the acronym "TOF". The data products with the word "Ion" in them are usually dominated by electrons. These "ion" data products contain the word "ion" only because they come from the SSD's that are used to measure ions with the coincident TOF process.

3. The energy channels of the three JEDI instruments do not exactly match each other because of the variations in the responses of different solid state detectors (SSD). Within each instrument there was a major effort to choose SSDs that matched each other in their responses (small differences remain). But between the different instruments there are noticeable differences. In order to plot combines spectra, some resampling is necessary. In the software that is internal to the JEDI team for plotting, one may choose native bins (which can give some choppy looking spectra because of the channel mismatches), "fuzzy bins" that resamples to generate a compromise between the channels of the multiple units, or completely resampled logarithmically spaced bins.

4. In the very strong magnetic field close to Jupiter, the size of the spacecraft is comparable to the electron gyro-radii. This causes the spacecraft to shadow observations of the electrons. The zero-order effect of this shadowing is a minimum in the apparent intensity of electrons near pitch angles of 90°. A labeled example of this effect can be found in Figure 8 of Mauk et al., (2020).

5. While we have no automated process for doing the full correction on the JEDI electron data as described in Text S1, we did decide mid-mission to start applying the high energy tail correction (Equation (1)) to the archived JEDI data. The data files (in the form of ASCII) generated since we started doing this correction as part of the processing have a keyword EFFCOR in the up-front meta data. If that parameter is set to T, the correction has already been applied. If it is set to F, or if that keyword is missing completely, the correction was

not applied. This is a reliable way to know for sure whether the high energy tail was corrected on a file-by-file basis.

6. Three parameters are reported for each energy channel: i) counts per accumulation, ii) counts per second, and iii) differential number Intensity. The counts per accumulation are raw counts, uncorrected by any knowledge of the response of the instrument to inputs. It can be used to assess statistical significance. It can be turned into a counts per second by dividing by the "duration" time (which usually is shorter than the interval between adjacent measurements due to multiplexing), also provided in the up-front information within each record. The recorded counts per second has had corrections applied to it to take into account the limitations in the instrument for counting particles (so-called "R versus R" corrections). The Intensity is calculated on the basis of this corrected counts per second. Note that the raw counts divided by duration will not match the recorded counts per second because of the corrections. When determining the statistical significant of a channel intensity averaged over time, it is important to remember to sum the counts per accumulation rather than to average them.

7. Ion energy is measured on the basis of solid-state-detector (SSD) pulses using two different techniques. Up to about 1.5 MeV the energy is measured on the basis of the height of the SSD pulses. Above about 1.5 MeV the energy is measured on the basis of the time-width of the pulses. This two-technique approach substantially increases the dynamic range for the measurements. However, the energy derived from the high energy pulse-width measurements is, as of this writing, less consistent between the different units, and overall is less calibrated than are the pulse height measurements.

8. For electrons with energies less than 30 keV, protons with energies less than 50 keV, and heavy ions less than 150 keV, the detector discrimination levels affect the efficiency of detection. As of this date, the intensities below these respective energies are uncalibrated, and provide intensities below the true values. At some point in time effort may be expended to calibrate the channels below those energies.

9. The Full-Width-at-Half Maximum (FWHM) angular resolution of the JEDI TOFxE and electron measurements is roughly $9°x17°$, with the $17°$ oriented along the $160°$ JEDI field-of-view. The TOFxPH data is not geometrically constrained by the SSDs, and its FWHM angular resolution is closer to $9°x30°$.

10. As the SSDs age with use and radiation, their noise levels at very low energies increase. We generally try to set detector signal thresholds to exclude this noise. However, sometimes we get behind in raising thresholds with the result that the very lowest energy channels have substantial false counts in them. To this date, the energy channels affected by detector noise have energies far below the energy measurements required of JEDI. That is, for electrons, the energy of the noise levels is far below 25 keV. Because of coincidence circuitry, the detector noise (always at fairly low values) does not affect the TOF ion measurements.

11. In addition to becoming noisy at the very lowest energies (item 10 above), another consequence of radiation forcing on SSDs is a minor loss of sensitivity. This loss of sensitivity causes the time-of-flight (TOF) x Energy (E) tracks to migrate to lower energies. Because the channelization of the ions into different species (H, He, O, S) are fixed at any one time based on the TOFxE characteristics, such migrations can cause different ion species to mix together in the data channels (particularly for O and S). This process is one of the reasons that onboard look-up tables are periodically updated.

12. Over the life of the mission, changes have been made to the on-board tables that modify the energy channels sampled. The beginning dates of each of four tables are: 2011-Day 235

(Table v0z),2015-Day104 (Table v1L), 2016-Day236 (Table v2f), and 2019-Day127 (Table v3a). The letters in the Table names track minor modifications to the tables. One of the key changes for the most recent update was to increase the energies that are sampled in the highest energy ion channels. There will be more table changes to come.

13. Periodically the high voltage on JEDI-90 and JEDI-270 trips off due to what are described as "micro-discharges" within the system. JEDI electronics senses these micro-discharges and commands the HV off just to make sure that the sensors are not damaged. While early in the mission these events required ground commands to restore the HV on the affected unit, presently the HV is turned on automatically after 12 hours.

14. There is one additional HV safety feature: when the micro-channel plate count rates rise above a (settable) threshold, the HV is reduced to a low value. Operational HV is restored the next time the HV is exercised on the spacecraft, typically during a spacecraft thrusting activity, which happens fairly often to maintain the spacecraft orientation. JEDI HV are turned down during these thrusting activities.

15. JEDI does not discriminate between Oxygen (O) and Sulfur (S) at energies below about 600 keV. Below that energy the O and S counts are combined (with intensities calculated as if these ions were oxygen). Above that energy there are separate O and S channels.

16. There are several issues of which one must be aware in using the low energy TOFxPH proton data. First, as discussed in Section s9, it is highly susceptible to accidental contamination. Second, the efficiency of detection decreases substantially with decreasing energy, as can be seen by comparing the "Intensity" and "Counts" profiles in Figure s7b. Sometimes a distribution on a spectrogram will look like an energy beam, whereas the truth is that the instrument just ran out of counts at the lower energies. Finally, the energy resolution decreases with deceasing energy, as seen in Figure 34 of Mauk et al. 2017a).

17. The heavy ion channels that are a part of the TOFxPH data have not been quantified, and much work remains to be done. Until proven otherwise, it must be assumed that these channels have some proton contamination within them.

18. As of this writing there are some minor anomalies in the archive data because of minor inadequacies in the calibration matrices utilized. For example, there are "hot" energy channels in the H+ TOFxE data near 60 keV and 90 keV channels that are anomalously high by 15-20%.

19. During recent perijoves (notable on PJ42 PJ46, PJ47, PJ48, but possible elsewhere) we occasionally find some corrupted spikes of data with count rates much higher (or negative) than are physically possible from the instrument. Because these spikes occur close to perijove but sometimes prior to the encounter of hard radiation, our working hypotheses is that these spikes are radiation-induced corruptions that occur after the data is transferred to the spacecraft mass memory and before the data is transmitted to Earth. It is important, at the highest time resolution, to filter out any such spikes with count rates higher than 5E6 [TBR] counts per second. It is, of course, possible that some corruption could be at a level that is not filterable with such a simple algorithm. It does not suffice to filter time-averaged data because the anomalous high rates get averaged together with much lower rates. The known corruptions are most readily identified in moments of the distributions (e. g. energy-integrated number intensity) where even a single bad channel input can generate unphysical results. At some point in time. once the corruptions are better understood, the archived Level-3 data will be filtered.

**Text S11. References**

Kollmann, P., et al. (2017), A heavy ion and proton radiation belt inside of Jupiter's rings, *Geophys. Res. Lett.*, 44, 5259– 5268, doi:10.1002/2017GL073730.

Mauk, B. H., and Fox, N. J. (2010), Electron radiation belts of the solar system, *J. Geophys. Res.*, 115, A12220, doi:10.1029/2010JA015660.

Mauk, B. H., Haggerty, D.K., Jaskulek, S.E. et al. (2017a), The Jupiter Energetic Particle Detector Instrument (JEDI) Investigation for the Juno Mission. *Space Sci Rev*, 213, Iss. 1-4, pp. 289-346, doi:10.1007/s11214-013-0025-3

Mauk, B. H., et al. (2017b), Juno observations of energetic charged particles over Jupiter's polar regions: Analysis of monodirectional and bidirectional electron beams. *Geophys. Res. Lett.*, 44, 4410–4418, doi:10.1002/2016GL072286.

Mauk, B. H., Haggerty, D. K., Paranicas, C., Clark, G., Kollmann, P., Rymer, A. M., … Valek, P. ( 2018). Diverse electron and ion acceleration characteristics observed over Jupiter's main aurora. *Geophysical Research Letters*, 45, 1277– 1285. https://doi.org/10.1002/2017GL076901

Mauk, B. H., Clark, G., Gladstone, G. R., Kotsiaros, S., Adriani, A., Allegrini, F., et al (2020b). Energetic Particles and Acceleration Regions over Jupiter's Polar Cap and Main Aurora; a Broad Overview. Journal of Geophysical Research: Space Physics, 125, e2019JA027699. https://doi.org/10.1029/2019JA027699

Paranicas, C., et al. (2017), Radiation near Jupiter detected by Juno/JEDI during PJ1 and PJ3, *Geophys. Res. Lett.*, 44, 4426– 4431, doi:10.1002/2017GL072600.

Paranicas, C., Mauk, B. H., Haggerty, D. K., Clark, G., Kollmann, P., Rymer, A. M., et al. (2018), Intervals of intense energetic electron beams over Jupiter's poles. *Journal of Geophysical Research: Space Physics*, 123, 1989– 1999. https://doi.org/10.1002/2017JA025106.

Zombeck, M. V. (2007), Handbook of Space Astronomy and Astrophysics, 3rd Edition, Cambridge University Press, Cambridge, U. K., ISBN-13: 978-0521782425, ISBN-10: 0521782422

**Table S1: Energy loss by protons in foils plus the 2 mm Al flashing on electron SSDs**

| Proton Energy (keV) | Electron Contam. Energy (keV) | Energy Lost (keV) |
|---|---|---|
| 200 | -112 | 311 |
| 223 | -76 | 299 |
| 249 | -37 | 286 |
| 278 | 6 | 272 |
| 310 | 52 | 259 |
| 347 | 102 | 244 |
| 387 | 157 | 230 |
| 433 | 216 | 216 |
| 483 | 281 | 202 |
| 540 | 351 | 189 |
| 603 | 427 | 176 |
| 673 | 510 | 163 |
| 752 | 600 | 151 |
| 839 | 699 | 140 |
| 938 | 808 | 129 |
| 1047 | 928 | 119 |
| 1169 | 1060 | 110 |
| 1306 | 1205 | 101 |
| 1459 | 1366 | 93 |
| 1629 | 1544 | 85 |
| 1820 | 1741 | 78 |
| 2032 | 1960 | 72 |
| 2270 | 2204 | 66 |
| 2535 | 2474 | 61 |
| 2831 | 2775 | 56 |
| 3162 | 3111 | 51 |
| 3532 | 3485 | 47 |
| 3945 | 3901 | 44 |
| 4406 | 4365 | 40 |
| 4920 | 4883 | 37 |
| 5495 | 5461 | 34 |
| 6138 | 6106 | 32 |

**Table S2: Fits to time-of-flight versus input energy in keV**

Time-of-Flight

Log10(TOF(ns)) = P6[Log10(Energy-into-sensor)]

|     | H        | He       | O        | S        |
| --- | -------- | -------- | -------- | -------- |
| a0  | 4.07022  | 6.67771  | 30.4431  | 22.8091  |
| a1  | -4.44458 | -9.48197 | -53.3389 | -36.9054 |
| a2  | 3.57637  | 8.05253  | 41.8469  | 27.7864  |
| a3  | -1.76968 | -3.81436 | -17.5368 | -11.2656 |
| a4  | 0.49005  | 0.996382 | 4.09294  | 2.55162  |
| a5  | -0.07096 | -0.13564 | -0.503966 | -0.30573 |
| a6  | 0.004173 | 0.007517 | 0.0255681 | 0.015132 |

**Table S3: Calculations from Table S2 showing time-of-flight versus input energy in keV**

|          |          | TOF in ns | TOF in ns | TOF in ns       | TOF in ns    |
| -------- | -------- | --------- | --------- | --------------- | ------------ |
| EN(keV)  | log10 EN | H         | He        | O               | S            |
| 4.65     | 0.67     | 181.81    | 963.40    | 1059770574.96   | 47654083.14  |
| 10.01    | 1.00     | 71.66     | 200.30    | 106192.38       | 48239.26     |
| 21.56    | 1.33     | 38.04     | 84.85     | 1272.75         | 1433.18      |
| 27.14    | 1.43     | 32.43     | 70.47     | 587.81          | 747.52       |
| 34.17    | 1.53     | 27.88     | 59.66     | 321.60          | 442.71       |
| 43.02    | 1.63     | 24.12     | 51.21     | 200.87          | 290.12       |
| 54.16    | 1.73     | 20.97     | 44.37     | 138.89          | 205.86       |
| 68.18    | 1.83     | 18.29     | 38.68     | 103.68          | 155.33       |
| 85.84    | 1.93     | 16.00     | 33.85     | 81.86           | 122.80       |
| 108.06   | 2.03     | 14.03     | 29.69     | 67.28           | 100.49       |
| 136.04   | 2.13     | 12.33     | 26.08     | 56.84           | 84.33        |
| 171.26   | 2.23     | 10.85     | 22.92     | 48.90           | 72.03        |
| 192.16   | 2.28     | 10.19     | 21.49     | 45.56           | 66.89        |
| 215.61   | 2.33     | 9.57      | 20.15     | 42.54           | 62.27        |
| 241.92   | 2.38     | 8.99      | 18.90     | 39.78           | 58.08        |
| 271.44   | 2.43     | 8.45      | 17.73     | 37.25           | 54.25        |
| 304.56   | 2.48     | 7.95      | 16.64     | 34.91           | 50.74        |
| 341.72   | 2.53     | 7.48      | 15.61     | 32.73           | 47.50        |
| 383.41   | 2.58     | 7.04      | 14.65     | 30.70           | 44.50        |
| 430.20   | 2.63     | 6.63      | 13.76     | 28.80           | 41.72        |
| 482.69   | 2.68     | 6.24      | 12.92     | 27.02           | 39.12        |
| 541.58   | 2.73     | 5.88      | 12.14     | 25.36           | 36.70        |
| 607.67   | 2.78     | 5.55      | 11.41     | 23.80           | 34.44        |
| 681.82   | 2.83     | 5.23      | 10.73     | 22.35           | 32.33        |
| 765.01   | 2.88     | 4.94      | 10.10     | 20.98           | 30.35        |
| 858.35   | 2.93     | 4.66      | 9.50      | 19.70           | 28.51        |
| 963.09   | 2.98     | 4.40      | 8.95      | 18.51           | 26.78        |
| 1080.60  | 3.03     | 4.15      | 8.43      | 17.39           | 25.16        |
| 1212.46  | 3.08     | 3.92      | 7.94      | 16.34           | 23.64        |
| 1360.40  | 3.13     | 3.71      | 7.49      | 15.37           | 22.22        |
| 1526.39  | 3.18     | 3.50      | 7.06      | 14.46           | 20.90        |
| 1712.64  | 3.23     | 3.31      | 6.66      | 13.61           | 19.65        |
| 1921.62  | 3.28     | 3.13      | 6.29      | 12.81           | 18.49        |
| 2156.09  | 3.33     | 2.96      | 5.94      | 12.07           | 17.40        |
| 2419.17  | 3.38     | 2.80      | 5.60      | 11.37           | 16.38        |
| 2714.35  | 3.43     | 2.64      | 5.29      | 10.72           | 15.43        |
| 3045.56  | 3.48     | 2.50      | 5.00      | 10.11           | 14.53        |

**Table S4: Fits to input energy versus SSD deposit energy by species (keV).**

Log10[Input Energy] = P6[Log10(SSD Deposited Energy)]

|     | e        | H        | He       | O        | S        |
|-----|----------|----------|----------|----------|----------|
| a0  | 1.05307  | 1.25705  | 1.54463  | 1.2593   | 1.26368  |
| a1  | 0.14046  | 0.171718 | -0.34265 | 2.27329  | 2.42085  |
| a2  | -0.37383 | 0.087186 | 0.579905 | -2.62401 | -2.82329 |
| a3  | 0.647852 | -0.00453 | -0.18774 | 1.49633  | 1.63798  |
| a4  | -0.27455 | 0.027604 | 0.043237 | -0.40407 | -0.45697 |
| a5  | 0.049721 | -0.00954 | -0.00547 | 0.053539 | 0.063008 |
| a6  | -0.00335 | 0.000892 | 0.000268 | -0.00281 | -0.00345 |

**Table S5: Calculations of input energy versus SSD deposit energy by species using Table S4**

Log10[Input Energy] = P6[Log10(SSD Deposited Energy)]

| Deposit SSD En (keV) | log10[Deposit] | KeV Electrons | KeV Protons | KeV Helium | KeV Oxygen | KeV Sulfur |
|------|------|---------|---------|---------|---------|---------|
| 10.00 | 1.00 | 17.35 | 33.91 | 42.87 | 112.61 | 126.42 |
| 12.59 | 1.10 | 19.49 | 37.33 | 47.26 | 116.45 | 130.89 |
| 15.85 | 1.20 | 22.24 | 41.40 | 52.59 | 120.59 | 135.68 |
| 19.95 | 1.30 | 25.79 | 46.28 | 59.05 | 125.49 | 141.33 |
| 25.12 | 1.40 | 30.35 | 52.16 | 66.84 | 131.62 | 148.35 |
| 31.62 | 1.50 | 36.19 | 59.29 | 76.24 | 139.43 | 157.23 |
| 39.81 | 1.60 | 43.68 | 67.96 | 87.59 | 149.38 | 168.53 |
| 50.12 | 1.70 | 53.26 | 78.58 | 101.29 | 162.04 | 182.81 |
| 63.10 | 1.80 | 65.52 | 91.63 | 117.89 | 178.04 | 200.79 |
| 79.43 | 1.90 | 81.20 | 107.76 | 138.02 | 198.17 | 223.29 |
| 100.00 | 2.00 | 101.23 | 127.77 | 162.51 | 223.40 | 251.33 |
| 125.89 | 2.10 | 126.77 | 152.72 | 192.40 | 254.94 | 286.18 |
| 158.49 | 2.20 | 159.26 | 183.93 | 228.96 | 294.31 | 329.39 |
| 199.53 | 2.30 | 200.51 | 223.11 | 273.83 | 343.42 | 382.89 |
| 251.19 | 2.40 | 252.74 | 272.47 | 329.07 | 404.65 | 449.07 |
| 316.23 | 2.50 | 318.70 | 334.80 | 397.26 | 480.98 | 530.88 |
| 398.11 | 2.60 | 401.79 | 413.67 | 481.70 | 576.13 | 631.97 |
| 501.19 | 2.70 | 506.21 | 513.62 | 586.56 | 694.72 | 756.82 |
| 630.96 | 2.80 | 637.22 | 640.39 | 717.12 | 842.51 | 910.97 |
| 794.33 | 2.90 | 801.34 | 801.24 | 880.10 | 1026.64 | 1101.26 |
| 1000.00 | 3.00 | 1006.84 | 1005.28 | 1084.03 | 1255.96 | 1336.13 |
| 1258.93 | 3.10 | 1264.16 | 1263.87 | 1339.76 | 1541.43 | 1626.08 |
| 1584.89 | 3.20 | 1586.62 | 1591.19 | 1661.06 | 1896.69 | 1984.14 |
| 1995.26 | 3.30 | 1991.30 | 2004.81 | 2065.41 | 2338.70 | 2426.66 |
| 2511.89 | 3.40 | 2500.18 | 2526.44 | 2574.99 | 2888.59 | 2974.16 |
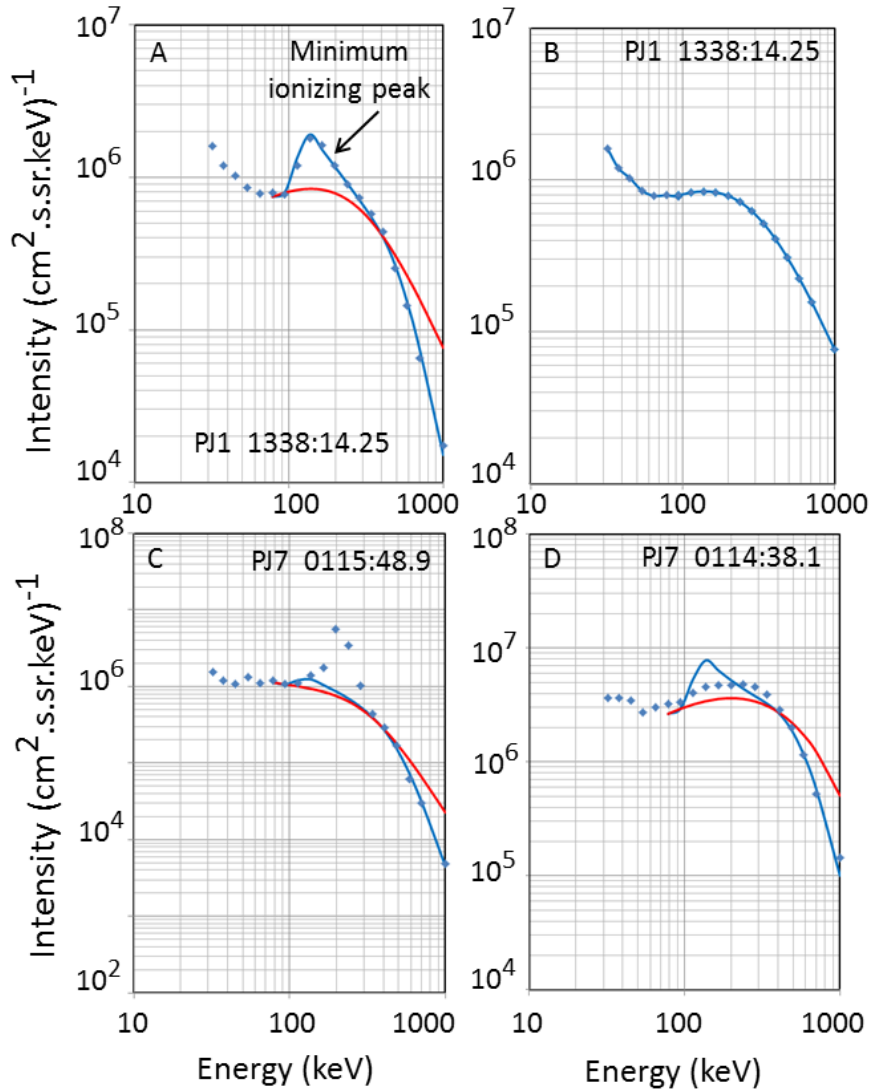
**Figure S1.** Electron differential number intensity energy spectra sample by the JEDI instrument (blue symbols) used to describe a procedure for correcting the spectra when contaminated by penetrating electrons (panels A and B), testing the degree of such contamination when the detector is seeing coherent auroral acceleration (panel C), and testing whether or not the JEDI sensor is partially saturated (panel D). Blue symbols are the JEDI channel measurements, blue lines are the fits to the measurements (Equation 5) and red lines are the modeled incoming electron spectra (Equation 3). See the text for details.
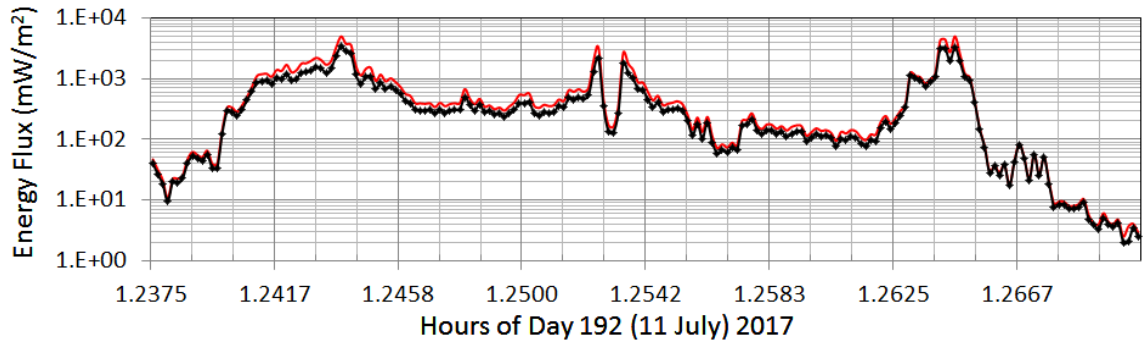
**Figure S2**. Low and high limit to the auroral energy flux, as described in Text S2
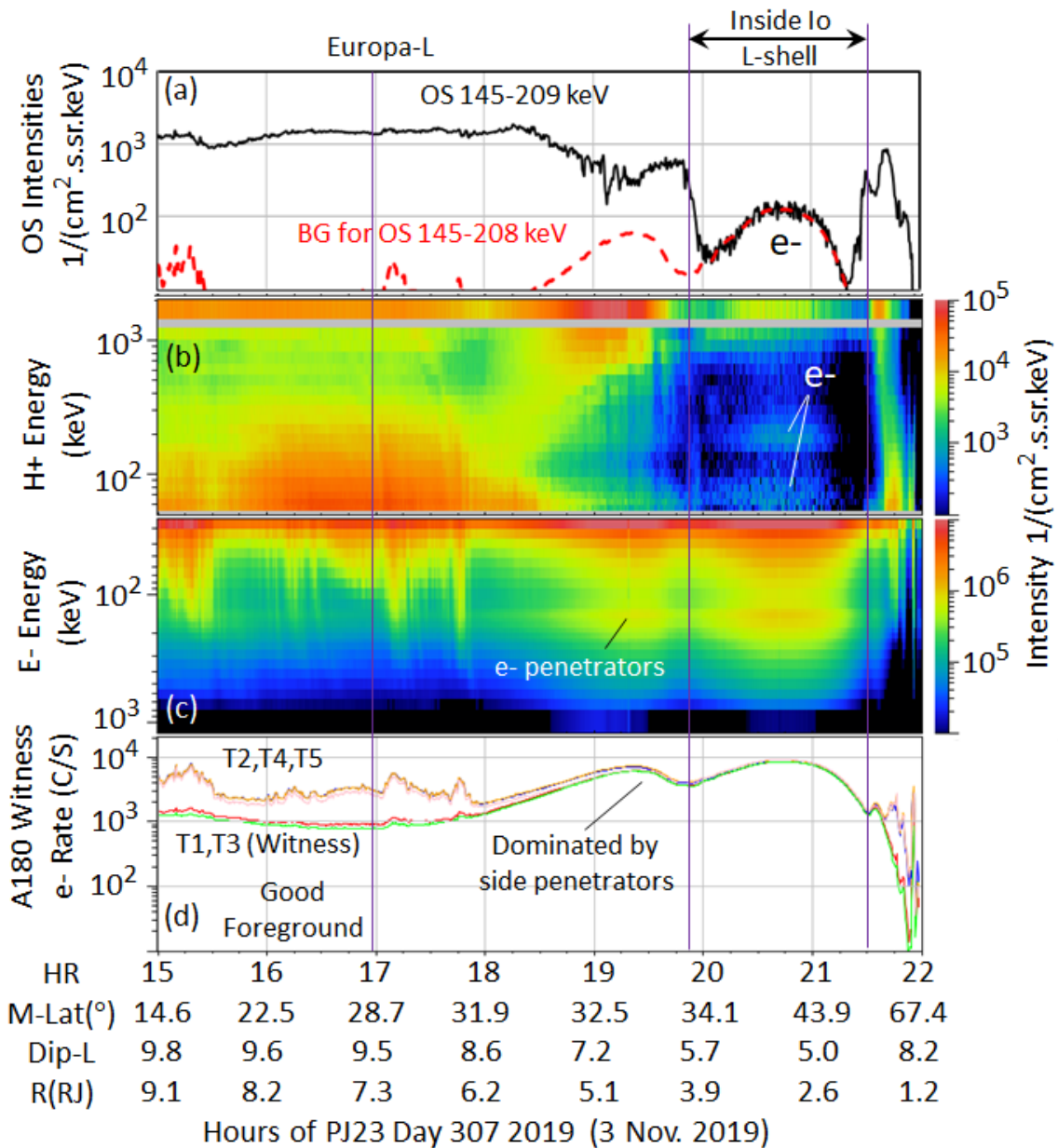
**Figure S3.** As described in Text S5, figure illustrating the use of the JEDI witness detectors (bottom panel) to determine when JEDI electron measurements are dominated by > 10-15 MeV electrons that penetrate the side walls of the JEDI instrument. Also, as discussed in Text S9, illustration of electron "accidentals" contamination of proton measurements (2nd panel) and heavy ion measurements (top panel).
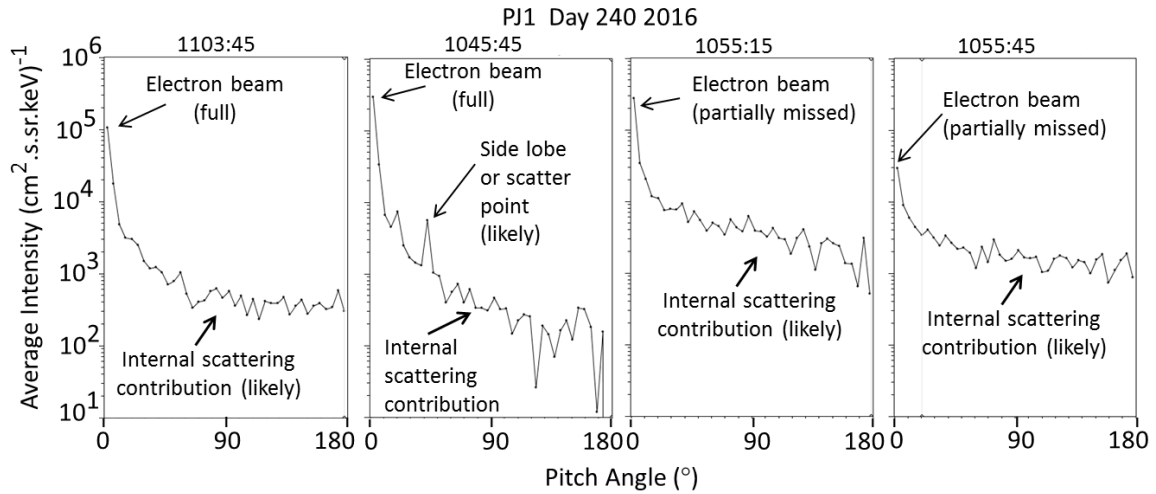
**Figure S4.** Electron pitch angle distributions measured by JEDI in the polar caps of Jupiter's polar regions where there are extremely narrow, upward going, magnetic field-aligned electron beams (Mauk et al., 2017a). This figure is intended to indicate that, because of internal scattering within the JEDI sensor volume, there are shoulders on the distributions that likely result from internal scattering rather than from electrons entering the sensor from those off-beam directions. These distributions are the energy-averaged differential number intensities, averaged over 30 – 1000 keV.
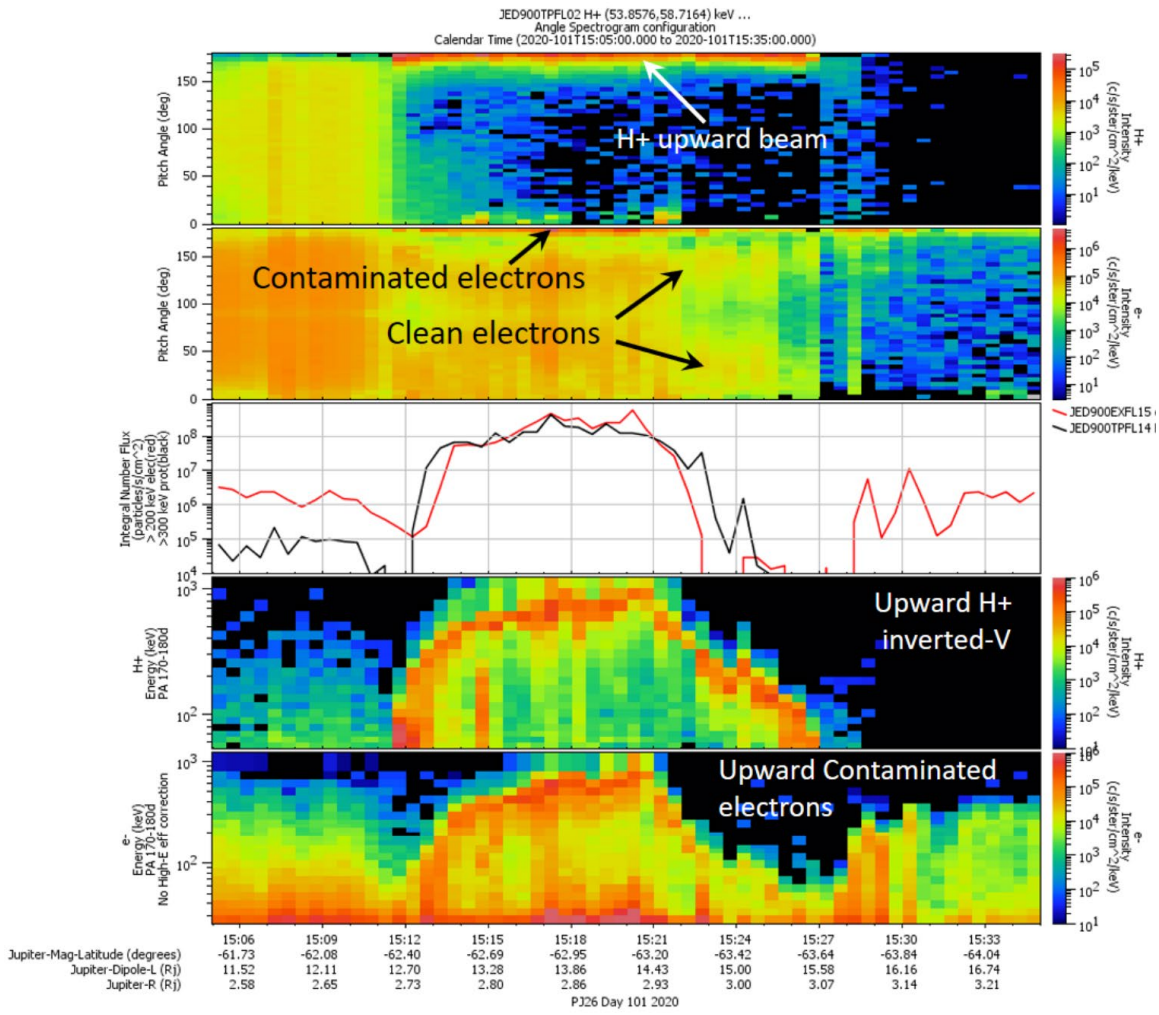
**Figure S5**. As described in Text S8, figure illustrating how energetic protons can very occasionally contaminate electron measurements.
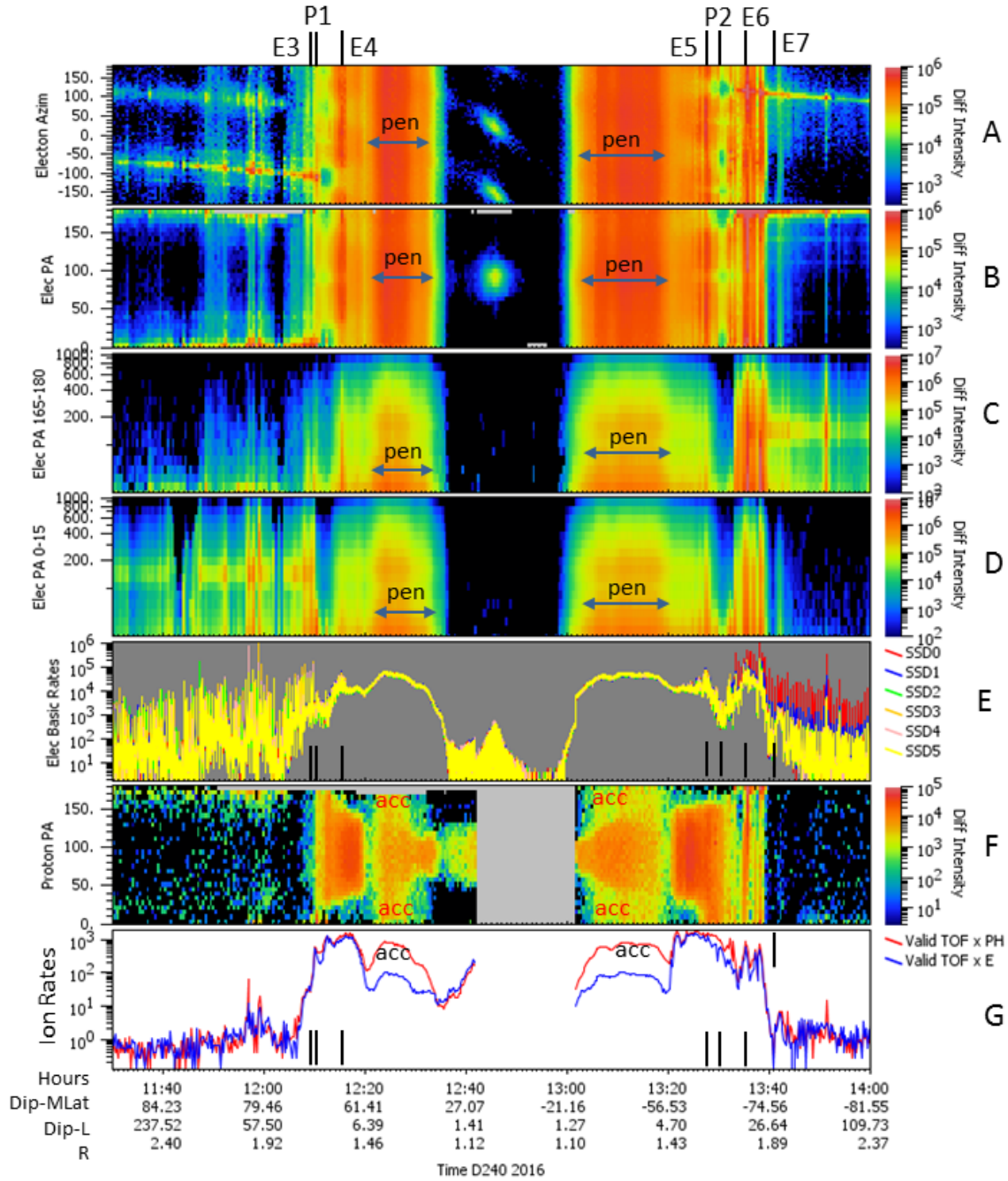
**Figure S6.** As described in Text S9, figure illustrating the occurrence of false populations resulting from contamination by electron-induced accidentals in the ion measurements, as revealed in the bottom two panels. The ions labeled with "acc" are completely false at all pitch angles and energies.
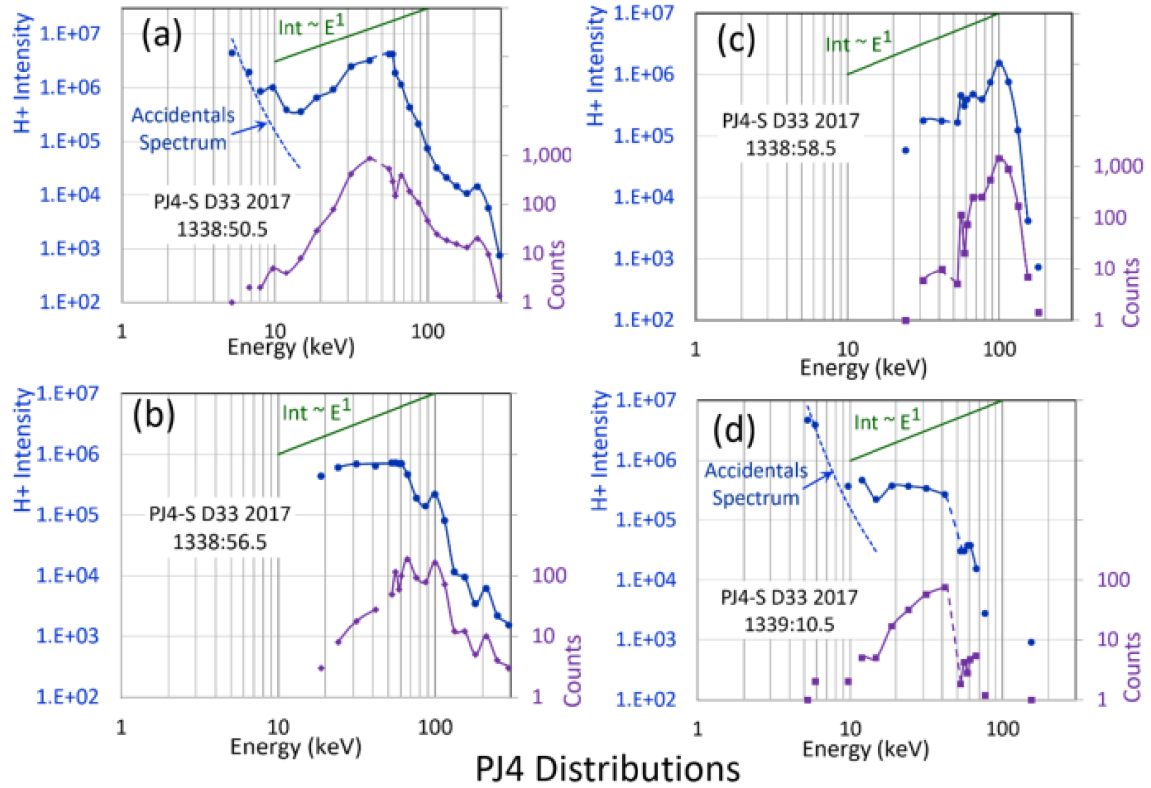
Figure S7. Selected proton upward propagating spectra that combine TOFxPH data (< 50 keV) and TOFxE data (> 50 keV) in a region over Jupiter's main aurora. Spectrum (b) demonstrates how the efficiency of TOFxPH measurements drops precipitously as the energy decreases (compare the intensities with the counts). Spectra (a) and (d) reveal the contamination at the lowest energies from "accidentals". The "universal" accidentals spectrum (Equation 9) has been place over the measured spectra there.